Nanoscale

ROYAL SOCIETY OF CHEMISTRY

PAPER

View Article Online
View Journal | View Issue

Published on 29 October 2021. Downloaded by University of Illinois - Urbana on 12/5/2021 5:25:19 PM.

Cite this: *Nanoscale*, 2021, **13**, 19587

Atomically thin telluride multiheterostructures: toward spatial modulation of bandgaps†

Zheng Hao,‡[a] Kai Xu,‡[a] Junzhe Kang,‡[a] Changqiang Chen[b] and Wenjuan Zhu *[a]

Received 10th June 2021,
Accepted 28th October 2021

DOI: 10.1039/d1nr03746c

rsc.li/nanoscale

Lateral multiheterostructures with spatially modulated bandgaps have great potential for applications in high-performance electronic, optoelectronic and thermoelectric devices. Multiheterostructures based on transition metal tellurides are especially promising due to their tunable bandgap in a wide range and the rich variety of structural phases. However, the synthesis of telluride-based multiheterostructures remains a challenge due to the low activity of tellurium and the poor thermal stability of tellurium alloys. In this work, we synthesized monolayer $WSe_{2-2x}Te_{2x}/WSe_{2-2y}Te_{2y}$ ($x > y$) multiheterostructures *in situ* using chemical vapor deposition (CVD). Photoluminescence analysis and Raman mapping confirm the spatial modulation of the bandgap in the radial direction. Furthermore, field-effect transistors with the channels parallel (type I) and perpendicular (type II) to the multiheterostructure rings were fabricated. Type I transistors exhibit enhanced ambipolar transport, due to the low energy bridges between the source and drain. Remarkably, the photocurrents in type I transistors are two orders of magnitude higher than those in type II transistors, which can be attributed to the fact that the photovoltaic photocurrents generated at the two heterojunctions are summed together in type I transistors, but they cancel each other in type II transistors. These multiheterostructures will provide a new platform for novel electronic/photonic devices with potential applications in broadband light sensing, highly sensitive imaging and ultrafast optoelectronic integrated circuits.

Lateral multiheterostructures with spatially modulated bandgaps have many unique applications, such as color engineered displays, high-performance thermoelectric devices, and tunneling diodes.[1,2] Despite the well-recognized applications, the lack of growth and fabrication technology for such materials has long been the main bottleneck. The lateral epitaxy of III–V materials is restricted by the lattice matching to the substrate. Two-dimensional (2D) materials can address these issues due to their interlayer van der Waals bonding. Various lateral multiheterostructures based on 2D transition metal dichalcogenides (TMDs) have been synthesized by CVD and metal organic CVD (MOCVD) processes.[3–11] In particular, Zhang *et al.* showed that TMD multiheterostructures can be formed using a reverse flow during the temperature-swing stage in the sequential vapor deposition growth process.[7] Sahoo *et al.* demonstrated a one-pot synthesis of TMD multiheterostructures by changing the composition of the reactive gas environment in the presence of water vapour.[4] Coherent atomically thin multiheterostructures can also be grown by changing the chalcogen precursors in the MOCVD process.[5] Recently, van der Waals heterostructure arrays between metallic TMDs and semiconducting TMDs were demonstrated using selectively patterned nucleation sites on monolayer or bilayer semiconducting TMDs.[12]

However, most TMD multiheterostructures reported so far are based on binary sulfides and selenides.[13,14] Multiheterostructures based on ternary tellurides remain unexplored. Due to the low activity of tellurium and the poor thermal stability of tellurium alloys, it is very difficult to synthesize tellurium alloys using CVD.[15] Recently, we demonstrated that the $WSe_{2-2x}Te_{2x}$ ternary alloy can be synthesized using a fast cooling process.[16] Since WTe_2 is a semimetal with a zero bandgap and WSe_2 is a semiconductor with a wide bandgap (1.61–1.65 eV for a monolayer),[17,18] the $WSe_{2-2x}Te_{2x}$ ternary compound has a tunable bandgap from ~1.44 eV to ~1.64 eV,[19] covering a broad range of the electromagnetic spectrum.

In this paper, we report the successful growth of monolayer $WSe_{2-2x}Te_{2x}/WSe_{2-2y}Te_{2y}$ multiheterostructures using the CVD method. The photoluminescence (PL) line scans show the periodic modulation of the bandgap as the flake grows laterally from the core to outer rings. Furthermore, transistors were fab-

[a]Electrical and Computer Engineering, University of Illinois at Urbana-Champaign, Urbana, IL 61801, USA. E-mail: wjzhu@illinois.edu
[b]Materials Research Laboratory, University of Illinois at Urbana-Champaign, Urbana, IL 61801, USA

† Electronic supplementary information (ESI) available. See DOI: 10.1039/d1nr03746c

‡ These authors contributed equally.

This journal is © The Royal Society of Chemistry 2021

Published on 29 October 2021. Downloaded by University of Illinois - Urbana on 12/5/2021 5:25:19 PM.

ricated on monolayer $WSe_{2-2x}Te_{2x}/WSe_{2-2y}Te_{2y}$ multiheterostructures with channel orientation parallel and perpendicular to the telluride rings. We found that the transistor with the channel parallel to the $WSe_{2-2x}Te_{2x}$ ring exhibits stronger ambipolar transport and a significantly higher photocurrent as compared to the transistor with the channel perpendicular to the $WSe_{2-2x}Te_{2x}$ ring.

The monolayer $WSe_{2-2x}Te_{2x}/WSe_{2-2y}Te_{2y}$ multiheterostructures were synthesized by precisely controlling the delivery of tellurium precursors and the temperature profile of the furnace. The schematic of the CVD system and the temperature profile of the furnace during the first- and second-round growth of the $WSe_{2-2x}Te_{2x}$ multiheterostructures are shown in Fig. 1a and b. The substrates and WO_3 precursor were placed at the center of the heating zone, while Te and Se precursors were placed near the edge of the heating zone. A movable boat carrying an additional Te precursor was placed outside the heating zone of the furnace. In the first-round growth, the temperature was first ramped up from room temperature to 600 °C within 20 minutes under a 90 sccm Ar flow and a low pressure of 25 mTorr. Then the temperature was raised to 760 °C within 10 minutes with a 9 sccm H_2 flow and was held for 7 minutes for nucleation and diffusion of the precursors. Next, the furnace was cooled down to 650 °C, followed by rapid cooling without the H_2 flow. The first-round growth with fast cooling enables the formation of a $WSe_{2-2x}Te_{2x}/WSe_{2-2y}Te_{2y}$ core/shell structure ($x > y$). Subsequently, the second-round growth was conducted *in situ*. The movable crucible with the additional Te precursor was pushed into the heating zone using an external magnet. This additional tellurium precursor was used to react with the residual WO_3 and selenium precursors and form the second $WSe_{2-2x}Te_{2x}/WSe_{2-2y}Te_{2y}$ lateral heterostructure. With repeated heating/cooling cycles, $WSe_{2-2x}Te_{2x}/WSe_{2-2y}Te_{2y}$ multiheterostructures were synthesized by sequential edge epitaxy. The optical images of the $WSe_{2-2x}Te_{2x}/WSe_{2-2y}Te_{2y}$ multiheterostructures are shown in Fig. 1c, which reveals the coexistence of alternating $WSe_{2-2x}Te_{2x}$ (dark) and $WSe_{2-2y}Te_{2y}$ (bright) domains. The topography image and the height profile across the flake obtained by atomic force microscopy (AFM) are shown in Fig. 1d. The height is uniform across multiple junctions, indicating the formation of seamless lateral multiheterostructures. Note that some pinholes exist on the flakes and substrate. These pinholes may come from the spin-coated perylene-3,4,9,10-tetracarboxylic acid tetrapotassium (PTAS), which was used to aid the nucleation of $WSe_{2-2x}Te_{2x}$ flakes.

Next, PL and Raman spectra were obtained from the center to the edge along the line marked in the optical image shown in Fig. 2a and b. Single PL peaks associated with direct excitonic emissions from the flake were observed for $WSe_{2-2x}Te_{2x}/WSe_{2-2y}Te_{2y}$ multiheterostructures (Fig. 2c). The contour plot of the normalized PL intensity as a function of the position from the center to edge is shown in Fig. 2e. The evolution of the distinct excitonic transitions between each crystal domain can be clearly observed. Across the first junction (from zone 1 to zone 2), the PL peak shifts from 1.44 eV (corresponding to $WSe_{2-2x}Te_{2x}$) to 1.53 eV (corresponding to $WSe_{2-2y}Te_{2y}$). At the second junction (from zone 2 to zone 3), the PL peak jumps

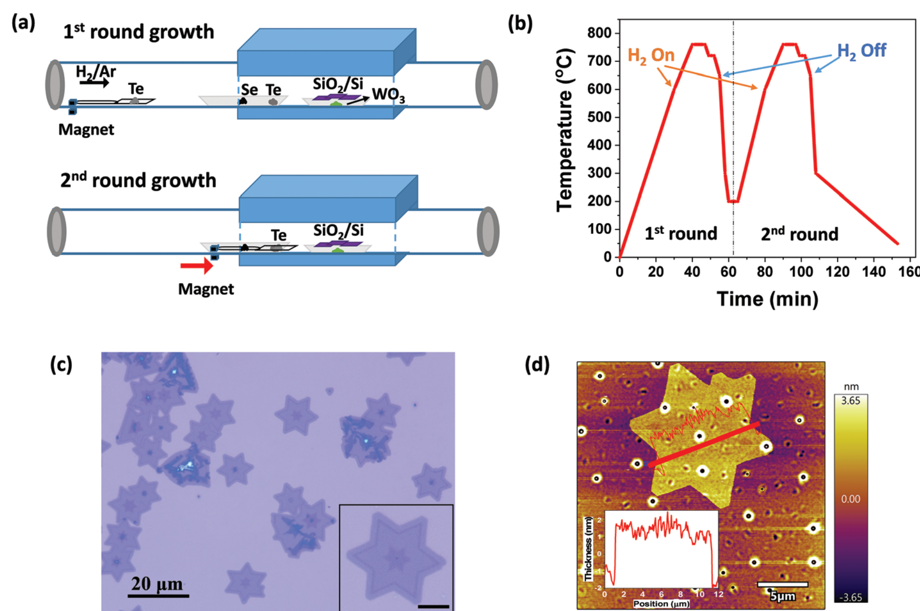

Fig. 1 Synthesis of monolayer $WSe_{2-2x}Te_{2x}/WSe_{2-2y}Te_{2y}$ multiheterostructures using the CVD system with a magnetically controlled crucible. (a) The schematic of the CVD system during the first and second round of growth. (b) The temperature profile of the furnace. (c) The optical image of the multiheterostructures. The inset shows the zoom-in image of a multiheterostructure flake. The scale bar in the inset is 5 μm. (d) AFM topography image of the $WSe_{2-2x}Te_{2x}/WSe_{2-2y}Te_{2y}$ multiheterostructure. The scale bar is 5 μm. The inset shows the height profile across the flake taken along the red line.

This journal is © The Royal Society of Chemistry 2021

Published on 29 October 2021. Downloaded by University of Illinois - Urbana on 12/5/2021 5:25:19 PM.

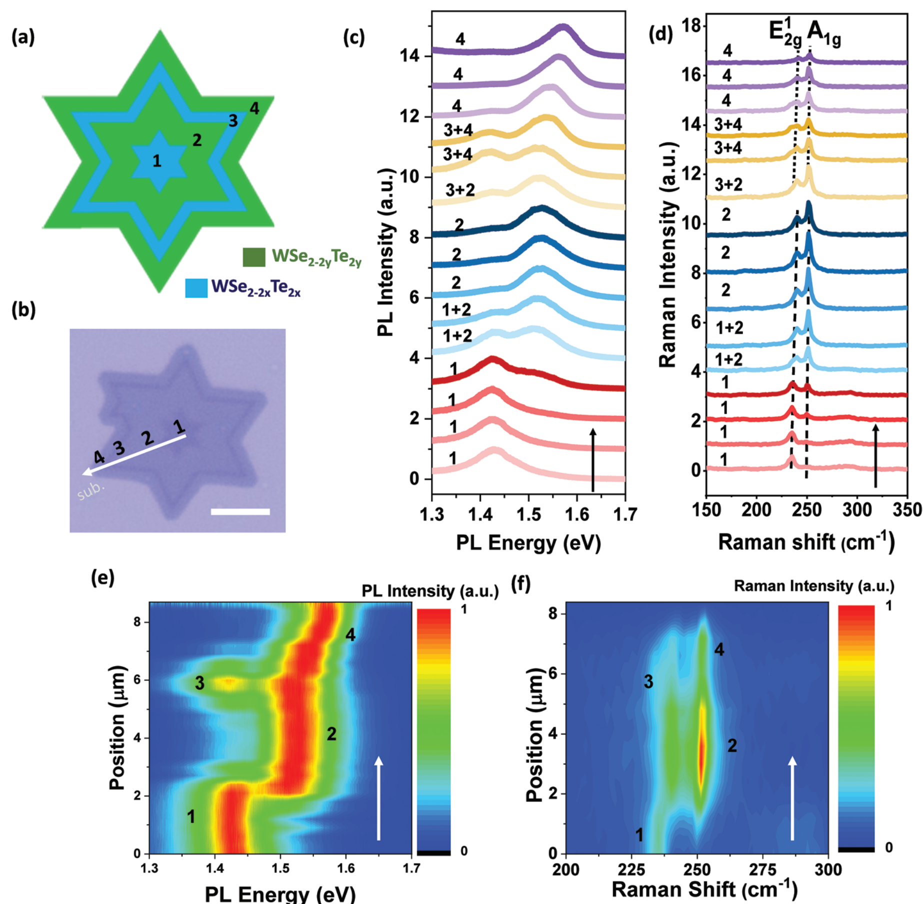

Fig. 2 Characterization of monolayer $WSe_{2-2x}Te_{2x}$/$WSe_{2-2y}Te_{2y}$ multiheterostructures. (a) Illustration and (b) optical image of the $WSe_{2-2x}Te_{2x}$/$WSe_{2-2y}Te_{2y}$ multiheterostructure. The scale bar is 5 μm. (c) PL spectra and (d) Raman spectra taken from the center (zone 1) to the edge (zone 4) of the multiheterostructure, as marked in (b). (e) Normalized PL and (f) normalized Raman contour plots along the direction perpendicular to the interfaces, where the arrow indicates the growth direction (from the center to the edge).

back from high energy to low energy. At the interfaces of two zones, the PL spectra are characterized by the co-existence of both peaks, which is due to the laser spot (~1 μm diameter) in the confocal microscope simultaneously probing both sides of the interface. Furthermore, the Raman line scan across the junctions (Fig. 2d) and the contour plot (Fig. 2f) exhibit a periodic shift of the Raman peaks. As the laser spot moves from $WSe_{2-2x}Te_{2x}$ (zone 1 and 3) to $WSe_{2-2y}Te_{2y}$ (zone 2 and 4), the E_{2g}^{1} peak blue-shifts, while the intensity of the A_{1g} peak is enhanced, which are consistent with previous reports.[19] Similar trends were observed in the PL and Raman contour plots obtained for other flakes grown in different batches, as shown in Fig. S1.† These results indicate that the growth of the $WSe_{2-2x}Te_{2x}$/$WSe_{2-2y}Te_{2y}$ multiheterostructure is repeatable and reproducible. The bandgap modulation of $WSe_{2-2x}Te_{2x}$/$WSe_{2-2y}Te_{2y}$ multi-heterostructures can be further widened by optimizing the growth parameters. For example, increasing the H_2 flow rate during the high-temperature growth period can facilitate the Te atoms to substitute the Se atoms, which will result in a higher Te concentration in zones 1 and 3. In addition, decreasing the cooling rate after the high-temperature growth can promote Se substitution of the Te atom, which will result in a higher Se concentration in zones 2 and 4.

The monolayer $WSe_{2-2x}Te_{2x}$/$WSe_{2-2y}Te_{2y}$ multiheterostructures enable multichannel devices. As illustrated in Fig. 3a, transistors with the channels parallel to the $WSe_{2-2x}Te_{2x}$ ring (type I) and perpendicular to the $WSe_{2-2x}Te_{2x}$ ring (type II) were fabricated. These two types of transistors present distinct electrical characteristics as shown in Fig. 3b. The type I transistor exhibits strong ambipolar transport, while the type II transistor shows p-type transport only. Moreover, the hole current of the type I transistor is higher than that of the type II transistor. These two types of transistors were fabricated side-by-side on the same flake. The dramatic difference in current transport between these two types of devices can be explained as follows. The tellurium concentration in the $WSe_{2-2x}Te_{2x}$ ring is higher than that in the $WSe_{2-2y}Te_{2y}$ region, which leads to a smaller bandgap in $WSe_{2-2x}Te_{2x}$. In addition, we found in the previous study that the hole Schottky barrier height in the $WSe_{2-2x}Te_{2x}$/Pd contact is larger than that in the $WSe_{2-2y}Te_{2y}$/Pd contact. Combining this information, we can construct the energy diagrams of the type I and type II transistors, as shown

Published on 29 October 2021. Downloaded by University of Illinois - Urbana on 12/5/2021 5:25:19 PM.

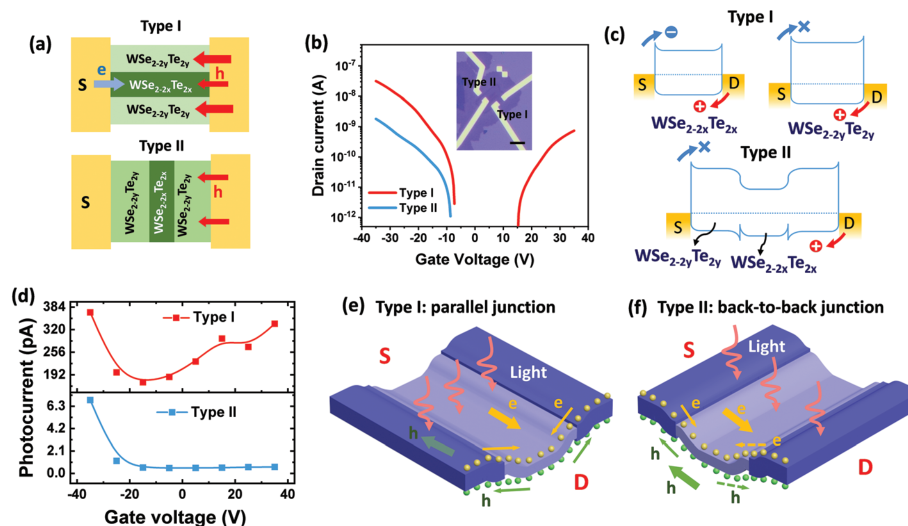

Fig. 3 The transistors based on the monolayer $WSe_{2-2x}Te_{2x}/WSe_{2-2y}Te_{2y}$ multiheterostructures. (a) The schematics of two types of transistors: the type I transistor has the channel parallel to the $WSe_{2-2x}Te_{2x}$ ring, while the type II transistor has the channel perpendicular to the $WSe_{2-2x}Te_{2x}$ ring. The red arrows depict the hole injection, while the blue arrow shows the electron injection when the drain voltage is positive. (b) The transfer curves of the type I and II transistors. Inset: The optical image of the type I and II transistors. The scale bar is 10 μm. (c) Energy diagrams of the type I and II transistors. (d) The photocurrents of the type I and II transistors. The type I transistor exhibits a significantly higher photocurrent as compared to the type II transistor. The diameter of the laser spot is 10.5 μm. The intensity of the laser is 7.5 W cm^{-2}. The width and length of the transistor channel are 2 μm. The drain voltage is 1 V. (e) and (f) 3D energy diagrams for type I and II transistors, respectively. In the type I transistor, the photogenerated carriers are separated by the built-in electric field and the carriers are collected along the pseudo-1D channels. In type II transistors, however, the photocurrents due to the photovoltaic effect generated at the two heterojunctions cancel each other.

in Fig. 3c. For the $WSe_{2-2y}Te_{2y}$/Pd contact, the low Schottky barrier for holes facilitates hole transport, while the large Schottky barrier for electrons limits the electron transport. In contrast, the band alignment between $WSe_{2-2x}Te_{2x}$ and Pd enables the simultaneous transport of both electrons and holes. In the type I transistor, the $WSe_{2-2x}Te_{2x}$ and $WSe_{2-2y}Te_{2y}$ sub-channels act as parallel bridges between the source and drain. The carriers can travel *via* any of these bridges. The Schottky barriers for holes at the $WSe_{2-2x}Te_{2x}$/Pd and $WSe_{2-2y}Te_{2y}$/Pd contacts are both low, so holes can be injected from the drain terminal to all three sub-channels (marked with red arrows). The Schottky barriers for electrons are low at the $WSe_{2-2x}Te_{2x}$/Pd contact, but high at the $WSe_{2-2y}Te_{2y}$/Pd contact; thus the electrons can be injected from the source terminal to the $WSe_{2-2x}Te_{2x}$ sub-channel (marked with a blue arrow), which leads to strong ambipolar transport. For the type II transistor, however, $WSe_{2-2x}Te_{2x}$ and $WSe_{2-2y}Te_{2y}$ zones are in series to each other. The carriers have to be injected through the $WSe_{2-2y}Te_{2y}$/Pd contacts. The large electron barrier at the $WSe_{2-2y}Te_{2y}/P_d$ contact prevents the electron injection and results in p-type transport. In addition, the source and drain terminals linked *via* zone 4 outside the channel region can also facilitate the hole transport. Note that hysteresis was observed in double-sweep transfer curves (Fig. S2†), which can be attributed to the traps at the dielectric/telluride interfaces.

The photoresponse of these two types of transistors was also dramatically different. The time evolution of the drain current was measured under the pulses of laser illumination at various gate voltages, as shown in Fig. S3.† In all cases, the drain current shows periodical modulation by light. The photocurrents were extracted by subtracting the laser-on currents from the laser-off currents and plotted as a function of gate voltage, as shown in Fig. 3d. The photocurrent of the type I transistor is about two orders of magnitude higher than that of the type II transistor. This enhanced photocurrent can be explained by the energy diagrams shown in Fig. 3e and f. In type II transistors, since the built-in electric fields at the two junctions have opposite directions, the photocurrents due to the photovoltaic effect at the two heterojunctions have the same magnitude but opposite polarity. These two current components will cancel each other, as shown in Fig. 3f. The photocurrent due to the photoconductive effect at the two heterojunctions is in the same direction. However, the back-to-back heterojunctions acted as a series of energy barriers and the rectifying effect will degrade the photocurrent. In contrast, for type I transistors, the electrons and holes generated by light at the two heterojunctions will be separated into two sub-channels by the built-in electric field. The electrons will be collected by the $WSe_{2-2x}Te_{2x}$ region and flow along the $WSe_{2-2x}Te_{2x}$ sub-channel to the drain, while holes will flow along the $WSe_{2-2y}Te_{2y}$ sub-channel. Here the electrons generated at the two heterojunctions will flow in the same direction following the lateral electric field between the source and drain. The sum of these two photocurrent components leads to an enhanced overall photocurrent. Furthermore, each heterojunction acts as a pseudo-one-dimensional energy bridge between the source and drain terminals, by which electrons

 This journal is © The Royal Society of Chemistry 2021

Published on 29 October 2021. Downloaded by University of Illinois - Urbana on 12/5/2021 5:25:19 PM.

and holes are effectively separated and drifted along the nanowire-like energy bridges. Therefore, the photoresponsivity of the type I transistor is significantly improved as compared to that of the type II transistor. The photoresponsivity of the type I transistor can be further enhanced by reducing the density of traps in the dielectrics, minimizing the defects in the alloy, and optimizing the source/drain contacts. These multiheterostructures can also be integrated with ferroelectric materials to construct bipolar transistors and reconfigurable logic transistors.

In summary, lateral monolayer $WSe_{2-2x}Te_{2x}/WSe_{2-2y}Te_{2y}$ multiheterostructures consisting of multiple domains with distinct bandgaps were successfully synthesized using the CVD system with magnetic crucibles. The controlled delivery of precursors coupled with temperature modulation enables sequential edge-epitaxy and continuous assembly of planar multijunctions. The PL spectra show the periodic modulation of the bandgap in the flake from the center to edge regions. Furthermore, the transistors with the channel parallel to $WSe_{2-2x}Te_{2x}$ rings (type I) exhibit strong ambipolar transport and an enhanced photocurrent as compared to those with the channel perpendicular to the $WSe_{2-2x}Te_{2x}$ ring (type II). Our demonstration of the omnidirectional telluride multiheterostructure presents a powerful framework for the epitaxial synthesis of lateral multiheterostructures and the engineering of the local material properties. These multiheterostructures can serve as a unique material platform for novel electronic and optoelectronic devices.

Conflicts of interest

There are no conflicts to declare.

Acknowledgements

The authors would like to acknowledge the support from the Office of Naval Research (ONR) under grant NAVY N00014-17-1-2973 and the National Science Foundation (NSF) under grant ECCS 16-53241 CAR. The scanning transmission electron microscopy (STEM) measurement was carried out in the Materials Research Laboratory Central Research Facilities at University of Illinois.

Notes and references

1 A. L. Pan, W. C. Zhou, E. S. P. Leong, R. B. Liu, A. H. Chin, B. S. Zou and C. Z. Ning, Continuous Alloy-Composition Spatial Grading and Superbroad Wavelength-Tunable Nanowire Lasers on a Single Chip, *Nano Lett.*, 2009, **9**(2), 784–788.

2 C. Z. Ning, A. L. Pan and R. B. Liu, Spatially Composition-Graded Alloy Semiconductor Nanowires and Wavelength Specific Lateral-Multijunction Full-Spectrum Solar Cells, *IEEE Photovolt. Spec. Conf.*, 2009, 2289–2292.

3 M. Y. Li, Y. Shi, C. C. Cheng, L. S. Lu, Y. C. Lin, H. L. Tang, M. L. Tsai, C. W. Chu, K. H. Wei, J. H. He, W. H. Chang, K. Suenaga and L. J. Li, NANOELECTRONICS. Epitaxial growth of a monolayer WSe2-MoS2 lateral p-n junction with an atomically sharp interface, *Science*, 2015, **349**(6247), 524–528.

4 P. K. Sahoo, S. Memaran, Y. Xin, L. Balicas and H. R. Gutierrez, One-pot growth of two-dimensional lateral heterostructures via sequential edge-epitaxy, *Nature*, 2018, **553**(7686), 63–67.

5 S. Xie, L. Tu, Y. Han, L. Huang, K. Kang, K. U. Lao, P. Poddar, C. Park, D. A. Muller, R. A. DiStasio Jr. and J. Park, Coherent, atomically thin transition-metal dichalcogenide superlattices with engineered strain, *Science*, 2018, **359**(6380), 1131–1136.

6 Y. Zhang, L. Yin, J. Chu, T. A. Shifa, J. Xia, F. Wang, Y. Wen, X. Zhan, Z. Wang and J. He, Edge-Epitaxial Growth of 2D NbS2 -WS2 Lateral Metal-Semiconductor Heterostructures, *Adv. Mater.*, 2018, e1803665.

7 Z. Zhang, P. Chen, X. Duan, K. Zang, J. Luo and X. Duan, Robust epitaxial growth of two-dimensional heterostructures, multiheterostructures, and superlattices, *Science*, 2017, **357**(6353), 788–792.

8 X. Duan, C. Wang, J. C. Shaw, R. Cheng, Y. Chen, H. Li, X. Wu, Y. Tang, Q. Zhang, A. Pan, J. Jiang, R. Yu, Y. Huang and X. Duan, Lateral epitaxial growth of two-dimensional layered semiconductor heterojunctions, *Nat. Nanotechnol.*, 2014, **9**(12), 1024–1030.

9 Y. Gong, S. Lei, G. Ye, B. Li, Y. He, K. Keyshar, X. Zhang, Q. Wang, J. Lou, Z. Liu, R. Vajtai, W. Zhou and P. M. Ajayan, Two-Step Growth of Two-Dimensional WSe2/MoSe2 Heterostructures, *Nano Lett.*, 2015, **15**(9), 6135–6141.

10 Y. Gong, J. Lin, X. Wang, G. Shi, S. Lei, Z. Lin, X. Zou, G. Ye, R. Vajtai, B. I. Yakobson, H. Terrones, M. Terrones, B. K. Tay, J. Lou, S. T. Pantelides, Z. Liu, W. Zhou and P. M. Ajayan, Vertical and in-plane heterostructures from WS2/MoS2 monolayers, *Nat. Mater.*, 2014, **13**(12), 1135–1142.

11 X. Q. Zhang, C. H. Lin, Y. W. Tseng, K. H. Huang and Y. H. Lee, Synthesis of lateral heterostructures of semiconducting atomic layers, *Nano Lett.*, 2015, **15**(1), 410–415.

12 J. Li, X. Yang, Y. Liu, B. Huang, R. Wu, Z. Zhang, B. Zhao, H. Ma, W. Dang, Z. Wei, K. Wang, Z. Lin, X. Yan, M. Sun, B. Li, X. Pan, J. Luo, G. Zhang, Y. Liu, Y. Huang, X. Duan and X. Duan, General synthesis of two-dimensional van der Waals heterostructure arrays, *Nature*, 2020, **579**(7799), 368–374.

13 S. Xie, L. Tu, Y. Han, L. Huang, K. Kang, K. U. Lao, P. Poddar, C. Park, D. A. Muller, R. A. DiStasio and J. Park, Coherent, atomically thin transition-metal dichalcogenide superlattices with engineered strain, *Science*, 2018, **359**(6380), 1131.

14 Z. Zhang, P. Chen, X. Duan, K. Zang, J. Luo and X. Duan, Robust epitaxial growth of two-dimensional heterostructures, multiheterostructures, and superlattices, *Science*, 2017, **357**(6353), 788.

Published on 29 October 2021. Downloaded by University of Illinois - Urbana on 12/5/2021 5:25:19 PM.

15 S. J. Yun, G. H. Han, H. Kim, D. L. Duong, B. G. Shin, J. Zhao, Q. A. Vu, J. Lee, S. M. Lee and Y. H. Lee, Telluriding monolayer MoS2 and WS2 via alkali metal scooter, *Nat. Commun.*, 2017, **8**(1), 2163.
16 K. Xu, A. Sharma, J. Kang, X. Hu, Z. Hao and W. Zhu, Heterogeneous Electronic and Photonic Devices Based on Monolayer Ternary Telluride Core/Shell Structures, *Adv. Mater.*, 2020, **32**(47), 2002548.
17 T. Yan, X. Qiao, X. Liu, P. Tan and X. Zhang, Photoluminescence properties and exciton dynamics in monolayer WSe2, *Appl. Phys. Lett.*, 2014, **105**(10), 101901.
18 A. Kumar and P. K. Ahluwalia, Electronic structure of transition metal dichalcogenides monolayers 1H-MX2 (M = Mo, W; X = S, Se, Te) from *ab initio* theory: new direct band gap semiconductors, *Eur. Phys. J. B*, 2012, **85**(6), 186.
19 P. Yu, J. Lin, L. Sun, Q. L. Le, X. Yu, G. Gao, C.-H. Hsu, D. Wu, T.-R. Chang, Q. Zeng, F. Liu, Q. J. Wang, H.-T. Jeng, H. Lin, A. Trampert, Z. Shen, K. Suenaga and Z. Liu, Metal–Semiconductor Phase-Transition in WSe2(1-x)Te2x Monolayer, *Adv. Mater.*, 2017, **29**(4), 1603991.

This journal is © The Royal Society of Chemistry 2021